

A Sub-Pixel Multimodal Optical Remote Sensing Images Matching Method

Tao Huang, Hongbo Pan, *Member, IEEE*, Nanxi Zhou, and Shun Zhou

Abstract—High-accuracy matching of multimodal optical images is the basis of geometric processing. However, the image matching accuracy is usually degraded by the nonlinear radiation and geometric deformation differences caused by different spectral responses. To address these problems, we proposed a phase consistency weighted least absolute deviation (PCWLAD) sub-pixel template matching method to improve the matching accuracy of multimodal optical images. This method consists of two main steps: coarse matching with the structural similarity index measure (SSIM) and fine matching with WLAD. In the coarse matching step, PCs are calculated without a noise filter to preserve the original structural details, and template matching is performed using the SSIM. In the fine matching step, we applied the radiometric and geometric transformation models between two multimodal PC templates based on the coarse matching. Furthermore, mutual structure filtering is adopted in the model to mitigate the impact of noise within the corresponding templates on the structural consistency, and the WLAD criterion is used to estimate the sub-pixel offset. To evaluate the performance of PCWLAD, we created three types of image datasets: visible to infrared Landsat images, visible to near-infrared close-range images, and visible to infrared uncrewed aerial vehicle (UAV) images. PCWLAD outperformed existing state-of-the-art eight methods in terms of correct matching rate (CMR) and root mean square error (RMSE) and reached an average matching accuracy of approximately 0.4 pixels across all three datasets. Our software and datasets are publicly available at <https://github.com/huangtaocsu/PCWLAD>.

Index Terms— multimodal matching, optical images, phase congruency, template, accuracy, mutual structure

I. INTRODUCTION

With the rapid development of remote sensing sensors, optical images with different spectral ranges can capture diverse types of information and are widely applied in areas such as target detection [1], environmental monitoring [2], and disaster management and rescue [3]. However, significant nonlinear radiometric and geometric deformation differences in multimodal image data often degrade the image matching accuracy, constraining the effectiveness of photogrammetric geometric processing [4] and ultimately affecting the quality of remote sensing products and applications.

Optical imaging sensors, commonly deployed on satellite

and UAV platforms, typically include the visible, near-infrared, and short-wave infrared bands to capture ground object reflectance and thermal characteristics [5]. Visible to near infrared (VNIR) images typically have higher resolution and provide detailed texture and variations in light and shadow, but are highly sensitive to weather conditions [6]. However, infrared images are resistant to these interferences and reveal features that are challenging to detect with VNIR, but they have lower resolution and provide less texture information [7, 8]. Therefore, the high-precision fusion [9] of VNIR and infrared images enables complementary advantages, improving performance in applications such as infrastructure defect inspection [10, 11], precision agriculture [12], and image recognition and classification [13].

However, due to the differences in pixel intensity, gradient changes, and texture features of multimodal optical images, which decreases the correlation between multimodal optical images. Feature-based methods are popularly used on multimodal optical images, such as scale-invariant feature transform (SIFT) [14], radiation-insensitive feature transform (RIFT) [15], and the oriented filter-based matching (OFM) [16]. However, traditional feature matching methods are challenging for multimodal images. Most multimodal feature matching methods use PC [17] to extract features [18] since PC is illumination and contrast invariant. These methods are designed to make feature descriptors invariant to the deformations and radiation in multimodal images, improving the robustness of matching multimodal images. However, feature matching accuracy remains limited due to the intrinsic structured noise within the PC and the influence of nonlinear phase distortions. Area-based methods utilize some template matching metrics such as sum of squared differences (SSD) [19], normalized cross-correlation (NCC) [20], and mutual information (MI) [21] between multimodal images or PC maps, such as histogram of oriented phase congruency (HOPC) [22] and channel features of oriented gradients (SFOC) [23]. However, these template matching metrics [24] struggle to PC noise and nonlinear phase variations, and they only provide integer-pixel matching results.

This paper considers the effects of noise on structural information in PC. We perform template matching using PC maps computed without a noise filter to increase the number of correctly matched points. Additionally, considering multimodal nonlinear radiometric distortions can introduce further nonlinear phase variations in PC, we adopt the SSIM as the similarity metric, due to its robustness to nonlinear brightness changes and noise [24]. To further mitigate the influence of noise during the fine matching process, we

This study was supported by the National Natural Science Foundation of China project (Nos. 42271410). (Corresponding author: Hongbo Pan).

Tao Huang, Hongbo Pan, Nanxi Zhou, and Shun Zhou are with the School of Geosciences and Info-Physics, Central South University, Changsha, China (email: huangtaosaf@csu.edu.cn; hongbopan@csu.edu.cn; nanxizhou@csu.edu.cn; zhoushuncsu@csu.edu.cn)

establish the correspondence between PC windows based on a mutual structure weighting strategy and a WLAD criterion for a robust sub-pixel offset estimate.

II. RELATED WORK

Existing methods for matching multimodal optical images can be broadly classified into three categories: feature-based methods, area-based methods, and data-driven methods based on deep learning [25, 26]. Feature-based matching methods are more flexible for large deformation scenarios than area-based methods. These methods typically involve three key steps: feature extraction, description, and matching. The main challenge is ensuring high repeatability of features during extraction and keeping distinctiveness and invariance during feature description in multimodal feature matching [27]. SIFT is a feature matching method for images of the same modality, typically constructed based on gradient information. However, the differences in pixel intensities and gradient distributions between multimodal images significantly diminish the effectiveness of traditional key points detection and description. In response, a series of improved SIFT-based methods were developed to address the challenges of multimodal feature matching. [28, 29]. Ma et al. and Xiang et al. aimed to enhance robustness by computing distinct gradients integrated within a gradient location and orientation histogram (GLOH)-like [30, 31] grid structure [32]. However, the discrimination of its descriptors will decrease. Area-based matching methods rely on the pixel intensity within a fixed-size template window to select the optimal template window. Template window similarity metrics often use SSD, NCC, and MI [33]. However, SSD and NCC have difficulty dealing with nonlinear radiometric distortions within image windows. MI is often used in medical image processing but involves complex computations and is sensitive to the window size [34].

Some dense matching studies have proved that template matching based on structural and shape information can create similarity maps of pixel-level features, suppress the effects of nonlinear radiation distortion [35, 36]. Ye et al. developed a descriptor using structural information and NCC to match similarity metrics. They later proposed a descriptor to improve computational efficiency, describing each pixel using oriented gradient information. On the one hand, although PC is robust to changes in brightness and contrast, nonlinear radiation differences still introduce nonlinear changes in PC. Methods such as HOPC are sensitive to these nonlinear variations, inconsistent modality responses, and noise. Meng et al. combined template matching with weights, multilevel local max-pooling, and max index backtracking to enhance the matching accuracy between UAV visible and infrared images [27]. Due to geometric distortions within the template window, the matching accuracy depends on the window size, which provides matching coordinates in integer pixels. Image filtering methods such as Log-Gabor [37] have been developed to calculate PC maps for feature detection and use the multi-scale and multi-directional filtering response to create descriptors resistant to nonlinear radiation distortions

[38]. Li et al. introduced RIFT [15], which detects key points using PC maximum moment and makes descriptors through a multi-scale, end-to-end loop structure to achieve rotation invariance. Based on this foundation, position-orientation-scale guided geometric and intensity-invariant feature transformation (POS-GIFT) [39] refined the filter weights across multiple orientations to generate more robust descriptors. Histogram of absolute phase consistency gradients (HAPCG) [40] uses anisotropic filtering to deal with nonlinear image diffusion, generating an anisotropic weighted moment map to calculate the histogram of absolute phase consistency gradients. Fan et al. observed that the maximum response index of the Log-Gabor filter in the direction produces consistent results across different modalities [41]. They proposed a coarse-to-fine matching framework called 3MRS [41]. Subsequently, they introduced the OFM [16] method to construct a rotation-invariant descriptor. Most feature descriptors in these multimodal matching algorithms exhibit strong robustness to nonlinear radiation differences and can be effectively applied to the multimodal image matching process. However, due to the presence of noise and nonlinear distortions in PC images, traditional feature detection methods struggle to ensure the accuracy and repeatability.

To achieve higher template matching accuracy, various optimization techniques are often developed. Adaptive least squares correlation (ALSC) [42] is commonly used to estimate the distortion transformation between matching windows, estimating sub-pixel displacement. To enhance the robustness of parameter estimation, some researchers have improved performance by providing better initial values [43] or optimizing the selection of weights through iterative refinement [44]. However, when nonlinear radiometric differences exist within the window, the combined effects of geometric deformation and noise prevent methods such as ALSC from obtaining reliable initial estimates. Consequently, these methods often fail to converge during iteration or produce results with many outliers. Data-driven matching algorithms have also advanced rapidly, with deep learning techniques being employed to learn and construct matching models from large-scale training datasets. Many researchers have explored their application to address the challenges of multimodal image matching [45, 46]. Single-stage deep neural networks can automatically learn feature descriptors or transformation model parameters [47-49]. To optimize the transformation parameters, Ye et al. leveraged emerging CNN architectures by fusing stimulus-based and CNN-extracted features within a simple similarity transformation framework [50], effectively utilizing mid- and high-level information for multispectral and multi-sensor image registration. Some researchers have also employed deep learning techniques to learn more reliable similarity metrics between descriptors [51]. SuperGlue [52] is a representative example that constructs a network for feature matching and outlier removal. The core idea is to reformulate the feature matching task as a differentiable optimization problem, enabling it to be solved using a graph neural network [53]. Kim et al. propose a novel network to enhance any detector with sub-pixel accuracy by

learning offset vectors of detected features [54]. End-to-end deep networks directly predict the underlying transformation model and typically adopt a fully automated, multi-scale, multimodal image matching framework [55]. Such frameworks generally consist of three neural network components: spatial feature extraction, feature description, and matching based on correlation functions in the feature space, as well as outlier rejection. LoFTR [56] represents a significant advancement in this field, achieving reliable matching even in low-texture regions. It performs feature detection, description, and matching at multiple scales, then refines dense correspondences at the sub-pixel level. LoFTR effectively generates robust feature descriptors for both

images by incorporating self-attention and mutual attention layers. Another category of end-to-end deep networks is the Generative Adversarial Network (GAN) [57]. Faced with extreme variations in real-world images, RoMa [58] integrates specialized convolutional neural network features (DINOv2) [59]. It builds a specialized fine feature pyramid and uses a custom transformer-based matching decoder to establish dense and robust matching. Deep learning-based multimodal matching significantly improves the robustness of feature correspondence and facilitates the identification of numerous matches [60]. However, it often suffers from low accuracy, unstable generalization across different datasets, and high training costs.

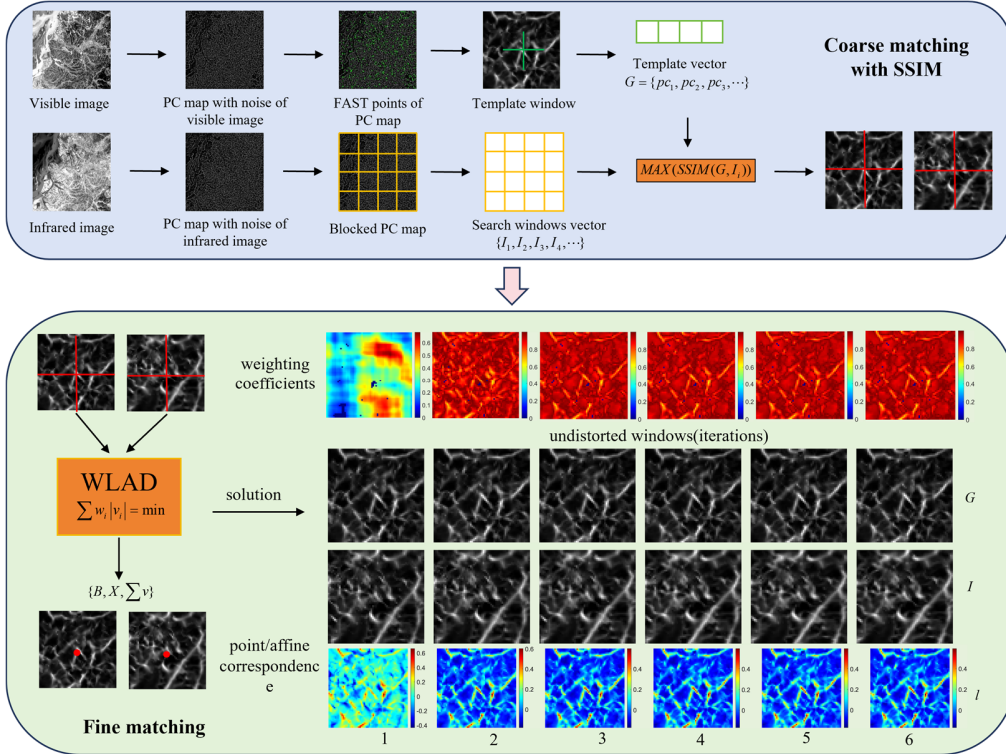


Fig. 1. Pipeline of the PCWLAD method.

III. METHODOLOGY

In this section, we propose a high-precision multimodal matching method for multimodal optical images, consisting of two main steps as shown in Fig.1. In the first step, considering that PC images are prone to structural degradation when noise is processed, we compute the PC without applying any noise filter, ensuring that the original structural information is retained. FAST [61] feature detection is performed on the visible PC image, which typically contains richer texture. A template window is selected around each detected feature point, and a corresponding search window is constructed on the thermal infrared PC map. Coarse matching is then performed using the SSIM as the similarity metric. In the second step, geometric and radiometric transformation between the coarse matched windows is established, and WLAD criterion is adopted to suppress noise and refine the

correspondences, achieving sub-pixel matching accuracy. A parameter-adaptive method [62] removes matching outliers.

A. Coarse matching based on SSIM

PC is widely used for feature matching in multimodal images due to its invariance to illumination and contrast, making it a robust choice for image analysis under varying imaging conditions. It quantifies the consistency of phase information across different frequency components at a given position after Fourier transformation, effectively highlighting salient structures independent of intensity variations. Kovessi refined the computational model of PC by employing Log-Gabor wavelets across multiple scales and orientations [63], enhancing its robustness and accuracy:

$$PC_2(x, y) = \frac{\sum_o \sum_n W_o(x, y) A_{no}(x, y) \Delta \Phi_{no}(x, y) - T_o}{\sum_o \sum_n A_{no}(x, y) + \varepsilon} \quad (1)$$

where (x, y) denote the coordinates of a point in the image, $W_o(x, y)$ is a weighting factor for a given frequency

distribution, $A_{no}(x, y)$ represents the amplitude at for wavelet scale n and orientation o , T_0 is the noise threshold, and ε is a small constant to prevent division by zero. $\Delta\Phi_{no}(x, y)$ is a more sensitive definition of phase difference.

However, a key challenge with PC is its sensitivity to noise, which can affect the stability and reliability of the response. Kovesi [63] considered noise as a random-phase Gaussian, where each vector in the summation consists of two independent normally distributed variables. Consequently, the position distribution of each vector follows a two-dimensional Gaussian distribution centered at the origin. The magnitude distribution of multi-scale energy vectors follows a Rayleigh distribution, which arises naturally when considering the Euclidean norm of two independent Gaussian-distributed components:

$$R(x) = \frac{x}{\sigma_G^2} e^{-\frac{x^2}{2\sigma_G^2}} \quad (2)$$

where σ_G^2 represents the variance of the Gaussian distribution describing the position of the total energy vector. The mean of the Rayleigh distribution is given by:

$$\mu_R = \sigma_G \sqrt{\frac{\pi}{2}} \quad (3)$$

Its variance is:

$$\sigma_R^2 = \sigma_G^2 \frac{4 - \pi}{2} \quad (4)$$

For the noise T_0 , it can be defined as:

$$T_0 = \mu_R + k * \sigma_R \quad (5)$$

where k is typically in the range 2 to 3.

However, PC aims to extract stable texture structures in multimodal matching. As a result, applying a fixed threshold is often challenging due to variations in local texture intensity. Additionally, in practical calculations, the mean and standard deviation of the Rayleigh distribution are estimated based on the response amplitudes across all positions in a given direction and multiple scales. This estimation can lead to excessive or insufficient noise suppression, potentially distorting local texture structures and ultimately affecting the accuracy and reliability of feature matching. As shown in Fig. 2, their structural consistency becomes challenging after the visible and infrared local PC maps are processed using the same noise method. However, the PC map without noise processing, although affected by noise, preserves the continuity and stability of edge textures relative to the original image, particularly in regions with prominent texture. Therefore, we mitigate noise during the matching process to preserve complete and meaningful texture information, enhancing the reliability and accuracy of the matching results.

To ensure the uniformity in the number and distribution of feature points, we apply FAST feature detection to the phase congruence map of the visible image without noise reduction. Utilizing the structural similarity of PC, we construct a square template window for each feature in the visible PC map with a neighborhood size of M , representing the phase values of all cells within the window as a vector G . In Fig.1, a search

window of the same size is constructed on the phase consistency map of the thermal infrared image, using the phase values within the window to form a vector I . The sliding window method is then employed to identify the template and search windows with the highest SSIM coefficient, achieving coarse matching.

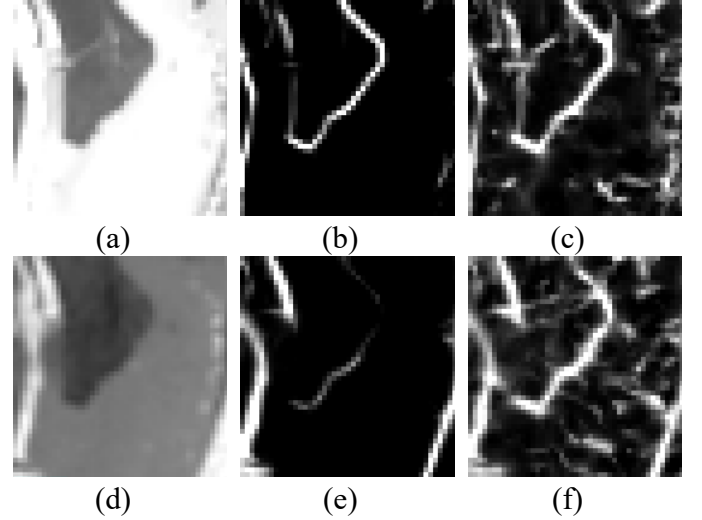


Fig. 2. Phase coherence noise. (a)A part of visible image;(b) Visible image PC after noise reduction;(c) Visible image PC without noise reduction;(d) A part of infrared image;(e) Infrared image PC after noise reduction;(f) Infrared image PC without noise reduction;

Considering the nonlinear radiometric differences between visible and infrared images, the PC map exhibits noise in the form of inconsistent texture structure responses. Additionally, the PC maps of the two modalities contain nonlinear components induced by the differences in radiation characteristics. The local SSIM index quantifies similarity based on three key elements: luminance similarity $L(G, I)$, which measures the consistency of brightness values between patches; contrast similarity $C(G, I)$, which evaluates variations in intensity. structural similarity $S(G, I)$, which captures the correlation of local structural patterns.

$$SSIM(G, I) = [L(G, I)]^\alpha \cdot [C(G, I)]^\beta \cdot [S(G, I)]^\gamma \quad (6)$$

α , β and γ are weights for luminance, contrast, and structure components, respectively. For luminance similarity, contrast similarity, and structural similarity, the definition is as follows:

$$L(G, I) = \frac{2\mu_G\mu_I + C_1}{\mu_G^2 + \mu_I^2 + C_1} \quad (7)$$

$$C(G, I) = \frac{2\sigma_G\sigma_I + C_2}{\sigma_G^2 + \sigma_I^2 + C_2} \quad (8)$$

$$S(G, I) = \frac{\sigma_{GI} + C_3}{\sigma_G\sigma_I + C_3} \quad (9)$$

Where μ_G and μ_I are the means of the G and I vectors respectively, σ_G and σ_I are the standard deviations of the G and I vectors respectively, σ_{GI} is the covariance of the G and I vectors. C_1 , C_2 and C_3 are stabilization constants that

prevent numerical instability when both $(\mu_G^2 + \mu_I^2)$ and $(\sigma_G^2 + \sigma_I^2)$ approach zero, ensuring reliable SSIM computations even in regions with low contrast or uniform intensity.

In general, $\alpha = \beta = \gamma = 1$. These components are computed using efficient and straightforward statistical measures and are then combined to formulate the local SSIM index:

$$SSIM(G, I) = \frac{(2\mu_G\mu_I + C_1)(2\sigma_{GI} + C_2)}{(\mu_G^2 + \mu_I^2 + C_1)(\sigma_G^2 + \sigma_I^2 + C_2)} \quad (10)$$

B. Fine matching with WLAD

To achieve higher matching precision, we perform fine matching based on the coarse matching results. A linear radiometric distortion model and an affine geometric distortion model are established between the template windows. However, due to the presence of noise in the PC map and potential deviations from the linear model, we incorporate mutual structure window data for weighting, as illustrated in Fig. 1. The parameters are then iteratively estimated using the criterion of least absolute deviation (LAD), ultimately converging to a sub-pixel coordinate matching result.

Given two square image windows $G(x', y')$ and $I(x'', y'')$, as illustrated in Fig. 1, where the coarse matching coordinates refer to the center of the windows. Window G can be mapped to window I through geometric and radiometric transformations.

$$\begin{aligned} & G(x', y') + e'(x', y') \\ &= r_0 + r_1 \cdot I(f_x(x', y'), f_y(x', y')) + e''(x'', y'') \end{aligned} \quad (11)$$

In general, the functions f_x and f_y can represent any two-dimensional coordinate transformation. r_0 and r_1 are the linear radiation correction parameters. e' and e'' represent the residual noise between the two image functions used to construct the geometric model. Since the geometric model defines a functional relationship between corresponding image template, the coordinates in window I can be expressed as a function of the coordinates in window G . Considering the imaging mechanisms of optical images, an affine model is typically employed:

$$\begin{cases} x'' = f_x(x', y') = a_0 + a_1x' + a_2y' \\ y'' = f_y(x', y') = b_0 + b_1x' + b_2y' \end{cases} \quad (12)$$

Where $a_0 \dots a_2$ and $b_0 \dots b_2$ are the affine coefficients. By linearizing the observation equation and incorporating weights w , the error equation can be constructed:

$$\begin{aligned} w^{1/2} \cdot v(x' + y') &= (c_1dr_0 + c_2dr_1 + c_3da_0 + \\ &c_4da_1 + c_5da_2 + c_6db_0 + c_7db_1 + c_8db_2 - l) \cdot w^{1/2} \end{aligned} \quad (13)$$

Where $c_1 \dots c_8$ are the observation coefficients.

Although SSIM can measure the similarity between two templates and demonstrates a certain level of noise robustness, it is ineffective in identifying which specific pixels within the window are affected by noise or the extent of the distortion. The nonlinear radiometric distortion between visible and infrared images often leads to inconsistent structural

responses, which can significantly disrupt the internal model of the window and hinder robust parameter estimation.

To mitigate the noise caused by inconsistent structural responses between multimodal optical images, the initial weights are computed based on the mutual structural similarity [64] of the PC values within the window. Linear regression relationship between patches G_N and I_N :

$$F(G_N, I_N, r_0, r_1) = \sum_{i \in N} (r_0 I_N + r_1 - G_N)^2 \quad (14)$$

This function linearly models the relationship between a patch in G_N and a corresponding patch in I_N . Here, N denotes the neighborhood size. We define $v(G_N, I_G)$ as the minimum error corresponding to the optimal values of r_0 and r_1 .

$$v(G_N, I_N)^2 = \min_{r_0, r_1} \frac{1}{|N \times N|} F(G_N, I_N, r_0, r_1) \quad (15)$$

$v(G_N, I_N)^2$ reaches the minimum when $r_1 = \sigma_{GI} / \sigma_G$ and $r_0 = \mu_{I_N} - r_1 \mu_{G_N}$. By simply substituting r_0 and r_1 into Eq. (15), the relation between the mean square error $v(G_N, I_N)$ and the structural measure $S(G, I)$ is:

$$v(I_p, G_p) = \sigma(G_N) \left(1 - S(I_N, G_N)\right)^2 \quad (16)$$

In this case, we take the I_N as the guidance image and G_N is the target. Following the same procedure, we construct:

$$v(I_N, G_N)^2 = \min_{h_0, h_1} \frac{1}{|N|} F(I_N, G_N, h_0, h_1) \quad (17)$$

We define our final patch mutual structure similarity measure as the sum of the two above functions defined symmetrically as:

$$MS(I_N, G_N) = v(I_N, G_N)^2 + v(G_N, I_N)^2 \quad (18)$$

According to Eqs. (15) and (16), and considering $S(I_N, G_N) = S(G_N, I_N)$, this measure boils down to:

$$MS(I_N, G_N) = \left(\sigma(I_N)^2 + \sigma(G_N)^2\right) \left(1 - S(I_N, G_N)\right)^2 \quad (19)$$

The weighting is performed by computing all mutual structures within the domain:

$$w_i = \frac{1}{M} \sum_{i \in M} MS(I_{N(i)}, G_{N(i)}) \quad (20)$$

The weighted least absolute deviation (WLAD) is used to minimize:

$$\min_x \sum_i w_i \cdot |v_i| = \min_x \sum_i w_i \cdot |B_i \cdot X - l_i| \quad (21)$$

Here, $X = [r_0, r_1, a_0, a_1, a_2, b_0, b_1, b_2]^T$ denotes the parameter to be estimated, $B_i = [c_1, c_2, c_3, c_4, c_5, c_6, c_7, c_8]$ is the observation coefficient matrix, l_i represents the i -th observation value, and w_i is the corresponding weight. Let W be a diagonal matrix with w_i as its diagonal elements and l is a vector composed of l_i .

The WLAD problem can be addressed using linear

programming techniques or iterative reweighted least squares approaches. Due to the nonlinearity of the original equation and the nature of the LAD solution, it is necessary to re-weight the observed data during the iterative process. Following the framework of iteratively reweighted least squares [65], the weights are determined based on the correlation between the model and the residuals d_i , thereby reducing the influence of noise outside the model.

$$w_i = \frac{1}{1 + |d_i|} \quad (22)$$

Finally, the parameters are estimated using the least squares method, and the iterative process terminates when the parameter change falls below a predefined threshold.

$$X = (BWB^T)^{-1}BWB^T l \quad (23)$$

IV. EXPERIMENT AND ANALYSIS

A. Datasets

Three optical multimodal images, comprising six image pairs, were used in the experiments, as shown in Figure 3. Landsat data: This dataset offers a registration accuracy better than 0.05 pixels [66, 67]. Small image patches were extracted to generate test samples, and additional resampled images with

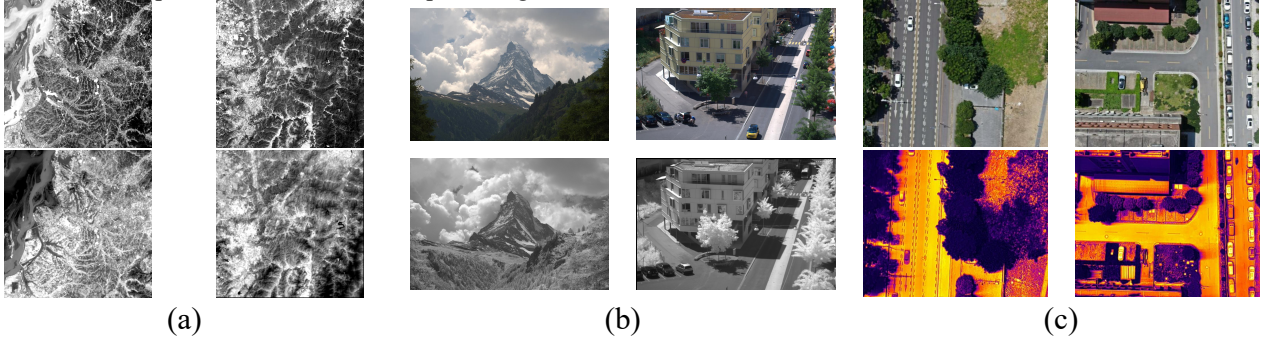


Fig. 3. Examples of three types of experimental data. (a)Landsat data. (b)BGRNIR data. (c)UAV data.

B. Evaluation Criteria and Parameter Settings

We present qualitative and quantitative experimental results to demonstrate the proposed method fully. The quantitative evaluation uses three indicators. (1) CMR is chosen as the evaluation criterion and is calculated as $CMR = C M/C$, where CM is the number of correct matched point pairs in the matching results, and C is the total number of matched point pairs. (2) To count the correct matches, we first use the obtained matches to estimate a transformation between an image pair. Then, the matches with residual errors of less than 2 pixels are taken as correct matches, and the number of correct matches is NCM. (3) Given a point (x_1, y_1) in one image, the corresponding epipolar line in the other image can be computed via the fundamental matrix, and the closest point (x_2', y_2') on this epipolar line represents the projection under epipolar geometry. The fundamental matrix H can be computed using equation (25). If the matching data have real coordinates, (x_2', y_2') can be considered a true point, and the use of H is unnecessary. If the coordinates of the

sub-pixel shifts were created. Landsat 8 and 9 data were primarily used in the experiment to make two pairs of test samples. Each image pair has a size of 512×512 pixels, with a ground sample distance (GSD) consistent with the thermal infrared data at 100 m. BGRNIR dataset: A dataset consisting of 477 registered color (RGB) and near-infrared (NIR) image pairs was used [68]. One image pair from a mountainous area and one from an urban area were selected. TIFF images with a resolution of 1024×768 pixels and sub-pixel offsets were added as test data. The images were captured using Nikon D90 and Canon T1i cameras equipped with B+W 486 (visible light) and 093 (NIR) filters. UAV Dataset: A custom UAV dataset was acquired using a DJI H20T camera, capturing visible and infrared images. The data were collected near the School of Geosciences and Info-Physics at Central South University. To improve the reliability of the accuracy assessment, overlapping visible and thermal infrared images taken from different viewpoints were carefully grouped. In addition, COLMAP [69] was used for bundle adjustment and image undistortion, resulting in a reprojection error of approximately 0.3 pixels. The complete dataset will be made available, with two selected subsets used for experimental comparative analysis. The UAV data are 648×516 pixels, with a GSD of 0.08 m.

corresponding matching point of (x_1, y_1) are (x_2, y_2) , RMSE can be calculated with equation (24). RMSE reflects the matching accuracy of the correct matches. The smaller the value of RMSE, the higher the accuracy. In addition, the image pairs with RMSE larger than two are deemed a matching failure.

$$RMSE = \sqrt{\frac{1}{NCM} \sum_{k=1}^{NCM} [(x_2^{k'} - x_2^k)^2 + (y_2^{k'} - y_2^k)^2]} \quad (24)$$

The accuracy of evaluation methods based on manual point selection is limited by the precision of the selected points and the inherent deformation characteristics of the images [22]. When remote sensing images are acquired from a near-vertical perspective, the influence of terrain-induced projection distortions is minimal, making an affine approximation feasible. However, in more complex scenarios, images may exhibit perspective distortion and projection differences caused by terrain undulations [70]. The fundamental matrix can be used in such cases for a more accurate estimation. The fundamental matrix describes the epipolar geometry between two images. For a 3D point in the same scene, its projections

in the two images are X_1 and X_2 , respectively. These projections satisfy the following relationship:

$$X_2^T H X_1 = 0 \quad (25)$$

H can be estimated by inputting the matching point coordinates into the RANSAC [71] algorithm, with the reprojection error threshold set to 2 pixels.

This section systematically analyzes the influence of three key factors on the proposed method. The first is the effect of PC noise processing on coarse matching; the second is the impact of using different similarity metrics on PC images for coarse matching; and the third is the influence of template size on coarse and fine matching. We extracted 1,000 FAST features from the visible PC image. We tested the method on two pairs of visible and infrared images from Landsat, two pairs of RGB and BIR images, and two pairs of visible and thermal infrared images from UAV platforms. The algorithm's performance was evaluated using CMR, RMSE, and convergence rate metrics.

We first evaluated the effect of PC noise processing on coarse matching, as illustrated in Figure 4. In most cases, the PC map (represented by the dotted line) exhibits a lower matching success rate than the PC map with noise. This trend is consistent across all four template matching criteria. Among them, the LAD criterion is most significantly affected by PC noise. As the template window size increases, the CMR of the noisy PC map approaches 100% on the Landsat dataset and around 95% on the WV03 dataset. For the UAV data, which is more affected by geometric distortion, the CMR reaches approximately 90%.

Regarding commonly used template matching criteria, we evaluated the performance of SSD, LAD, NCC, and SSIM on the PC map. As shown in Figure 4, SSIM generally achieves a higher CMR than the other three criteria. Across all three datasets, SSIM demonstrates better noise robustness, particularly when the template window is small, resulting in a higher CMR than NCC. However, as the window size increases, the CMR values of all four criteria gradually same, with SSIM maintaining a slight advantage.

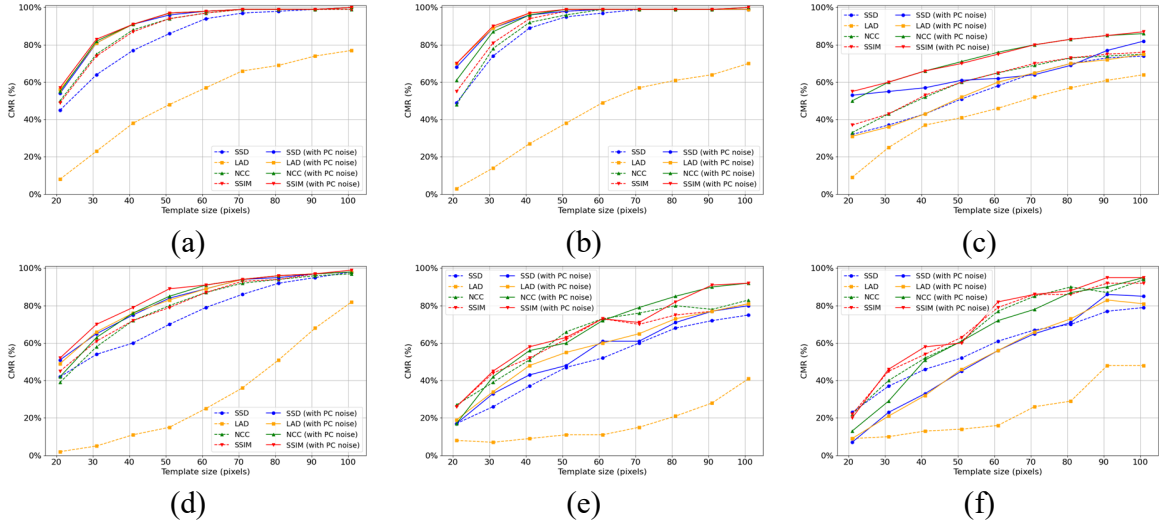


Fig. 4. Relationship between template size and CMR values for SSD, LAD, NCC, and SSIM in PC template matching, with and without noise processing. (a) Landsat visible-infrared 1. (b) Landsat visible-infrared 2. (c) BGR_NIR 1. (d) BGR_NIR 2. (e) UAV visible-infrared 1. (f) UAV visible-infrared 2.

As the template window size increases, Figure 4 shows that the accuracy of coarse matching gradually improves and tends to stabilize when the window reaches a size of 101. For fine matching, the matching accuracy also increases with window size on the Landsat and BGRNIR datasets. On the UAV datasets with particular geometric distortion, the lowest RMSE is observed when the window size reaches approximately 81, as shown in Figure 5(a). Considering the nonlinearity of the fine matching model, iterative optimization is required, and the convergence rate influences the final number of matched points. The convergence rate is defined as the ratio of the number of the NCM in the coarse matching stage to the NCM in the final fine matching result. As Figure 5(b) illustrates, the convergence rate increases across all three datasets as the window size grows. This improvement is primarily because larger windows contain more reliable structural and textural information, which helps mitigate the effects of noise.

Based on the above results, we adopt the noisy PC map for coarse matching and select SSIM as the template matching criterion. The neighborhood window size M for coarse

matching is set to 101, while the window size N for fine matching is set to 81, considering the matching accuracy across all datasets. The maximum number of iterations is set to 20 during the precision optimization process. The iteration terminates when the offset corrections Δa_0 and Δb_0 are less than 0.05 pixels, and the SSIM coefficient exceeds both 0.4 and the initial SSIM coefficient.

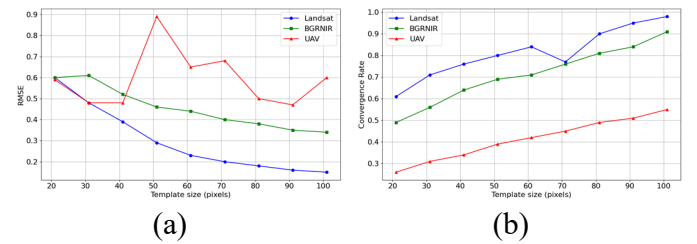


Fig. 5. The relationship between RMSE, convergence rate, and template size across different datasets. (a) Relationship between RMSE and template size. (b) Relationship between convergence rate and template size.

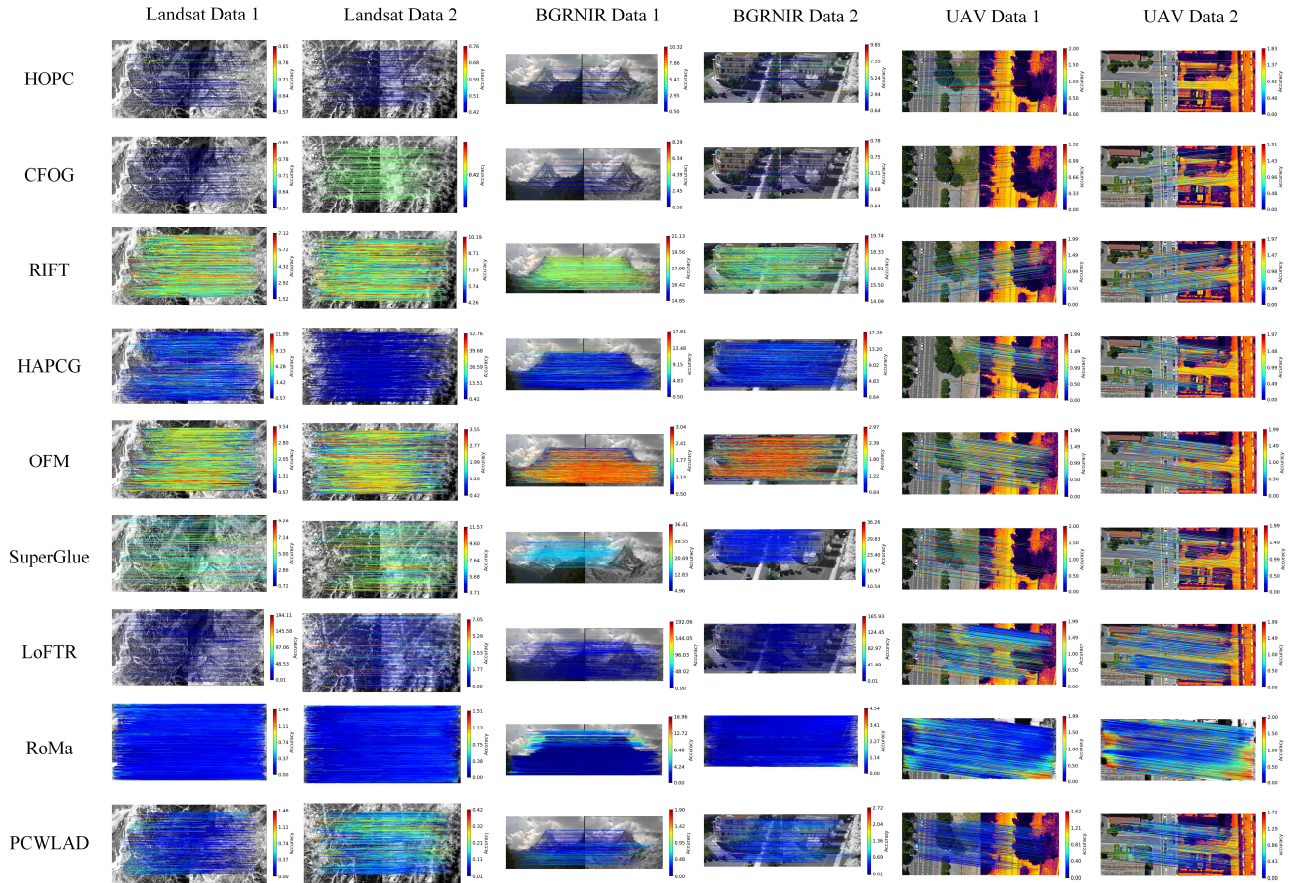


Fig. 6. Matching lines are plotted for each method. Different colors represent the RMSE of the matching points.

C. Qualitative results and analysis

This section qualitatively evaluates the performance of the proposed method using six pairs of optical multimodal remote sensing data. The method is compared against seven state-of-the-art approaches, including area-based methods (HOPC and CFOG), feature-based methods (RIFT, HAPCG, and OFM), and deep learning-based methods (SuperGlue, LoFTR and RoMa).

For qualitative evaluation, the matches identified by each method on six image pairs are visualized in Figure 6. Automatically and accurately matching these multimodal images is particularly challenging due to the significant radiometric differences. It can be observed that HOPC and CFOG demonstrate relatively stable performance across the six datasets, delivering whole-pixel matching results. However, they match only a small number of matching points, and notable mismatches are present in the BGR-NIR Data 1. While RIFT provides sufficient matches, it yields almost no correct correspondences in the Landsat and BGR-NIR datasets, resulting in low matching accuracy. Although many of the HAPCG matches are correct, many exhibit an RMSE deviation exceeding 2 pixels, indicating low CMR. OFM achieves higher accuracy than RIFT but still includes some incorrect matches. SuperGlue fails on the Landsat and BGR-NIR datasets, producing only mismatches, and also performs poorly on the remaining datasets. LoFTR still suffers from gross errors, but some matching points can achieve sub-pixel accuracy. However, the number of correct matches remains limited across these methods, and sub-pixel accuracy is generally

difficult to attain. In contrast, the proposed PCWLAD and RoMa achieve a high matching accuracy, with a significantly greater number of matching points than the area-based methods such as HOPC and CFOG.

On the other hand, we use two pairs of images with different perspectives to compute the fundamental matrix and evaluate accuracy based on the reprojection residuals, as shown in Figures 7 and 8. The two aerial images captured by the UAV conform to epipolar geometry. After relative orientation, the coordinate differences of corresponding points in the two images should obey the epipolar geometry, with residuals perpendicular to the epipolar line direction. The residuals are perpendicular to the baseline direction when the two images are taken from orthogonal views. Therefore, the residuals can be used to evaluate the matching accuracy, as illustrated in Figure 7. Under flat terrain conditions, it can be observed that CFOG, RoMa, and PCWLAD maintain residuals roughly perpendicular to the epipolar lines, indicating good internal consistency. In contrast, other methods fail to meet this constraint. In Figure 8, under conditions of significant perspective changes and undulating terrain, only the proposed PCWLAD method maintains residuals perpendicular to the epipolar lines, further demonstrating the superior internal consistency of our approach.

D. Quantitative indicator comparison and analysis

To ensure a fair and rigorous quantitative comparison, we evaluated the nine methods on six image pairs using three metrics: CMR, RMSE, and NCM. For RMSE computation,

only those matches with residuals less than 2 pixels were considered valid, i.e., only correct matches were included in the calculation. The statistical results in Figure 9 demonstrate that the proposed PCWLAD method outperforms all other methods across nearly all datasets. It highlights its effectiveness and advantages in high-precision matching of optical multimodal images. The CMR and accuracy of the matching results are significantly enhanced by incorporating noise suppression and optimization strategies applied to the PC maps.

According to the results shown in Figure 9(a), the CMR performance of the proposed PCWLAD method is remarkably stable, with values close to 100% across all datasets and minimal fluctuations. RoMa, HOPC, and CFOG achieve high CMR values with very low dispersion. The median CMR of LoFTR is slightly lower than that of HOPC, but still outperforms methods such as OFM and HAPCG. The CMR distributions of OFM and HAPCG fall within a moderate range, generally between 60% and 80%, indicating relatively stable performance. In contrast, RIFT and SuperGlue exhibit

significantly lower CMR values, with occasional matching failures. A comprehensive comparison of the average quantitative results for all three categories of image data is provided in Table I.

Table I and Figure 9(b) demonstrate that the proposed PCWLAD method achieves the highest accuracy among all evaluated methods. PCWLAD exhibits the smallest and most compactly distributed RMSE values, with an average RMSE of approximately 0.34 pixels across the three types of datasets. The average RMSE of RoMa across the three types of datasets is approximately 0.4 pixels, which is slightly better than that of the proposed PCWLAD on the Landsat and BGRNIR datasets in Table I. However, on real UAV data, RoMa's RMSE is about 0.3 pixels higher than PCWLAD's. CFOG, HOPC, and LoFTR also yield relatively low RMSEs with good stability, ranging between 0.6 and 0.9 pixels. In contrast, the RMSEs of OFM and HAPCG are notably higher, exceeding 1 pixel. SuperGlue and RIFT perform the worst in accuracy, showing the highest RMSEs and significant fluctuations across different datasets.

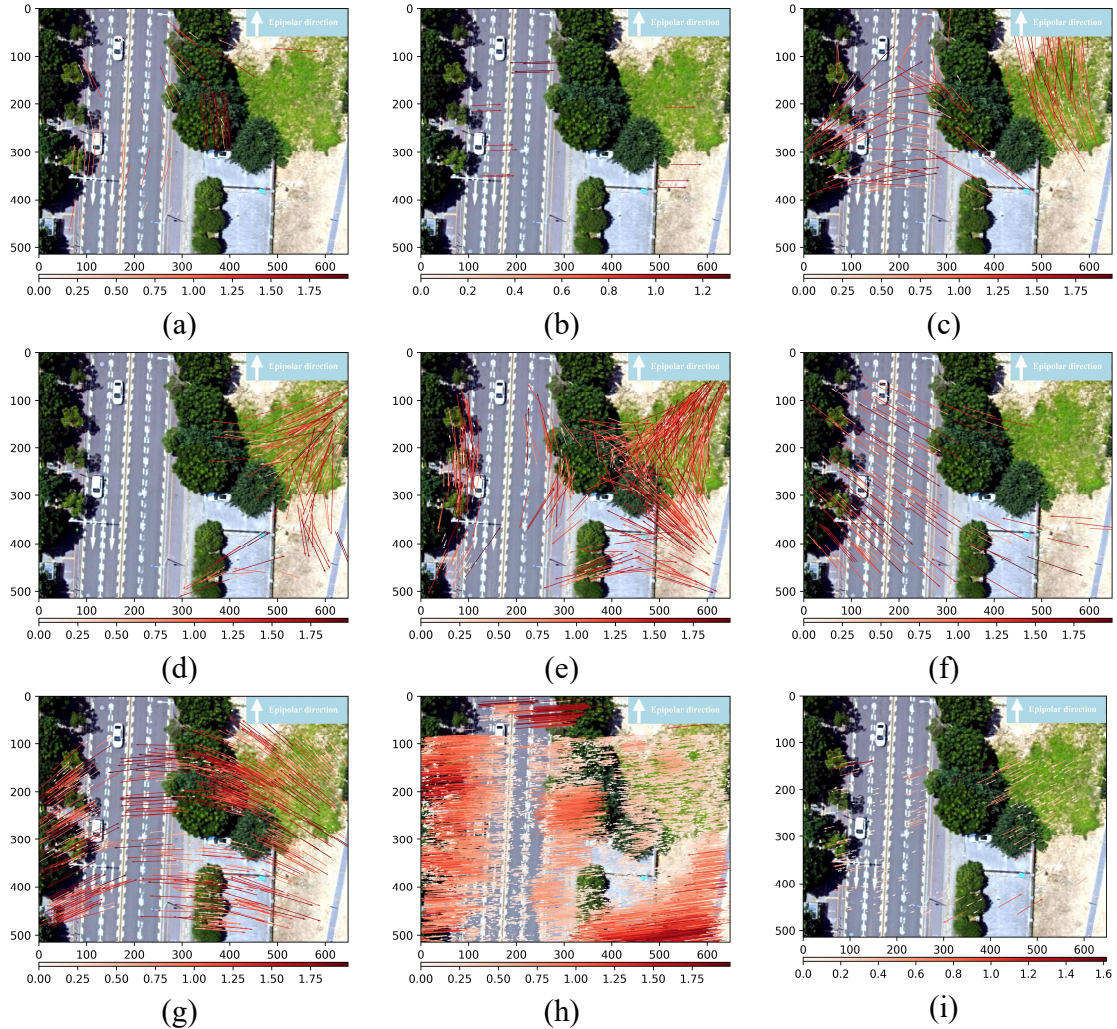


Fig. 7. The distribution of the residuals of the reprojection of the fundamental matrix of the nine methods on UAV data 1. The direction of the red arrow indicates the residual direction and size under the epipolar line constraint, and the color intensity indicates the residual size. The epipolar line direction is roughly consistent with the baseline direction. (a)HOPC results. (b)CFOG results. (c)RIFT results. (d)HAPCG results. (e)OFM results. (f)SuperGlue results. (g)LOFTR results. (h) RoMa results. (i) PCWLAD results.

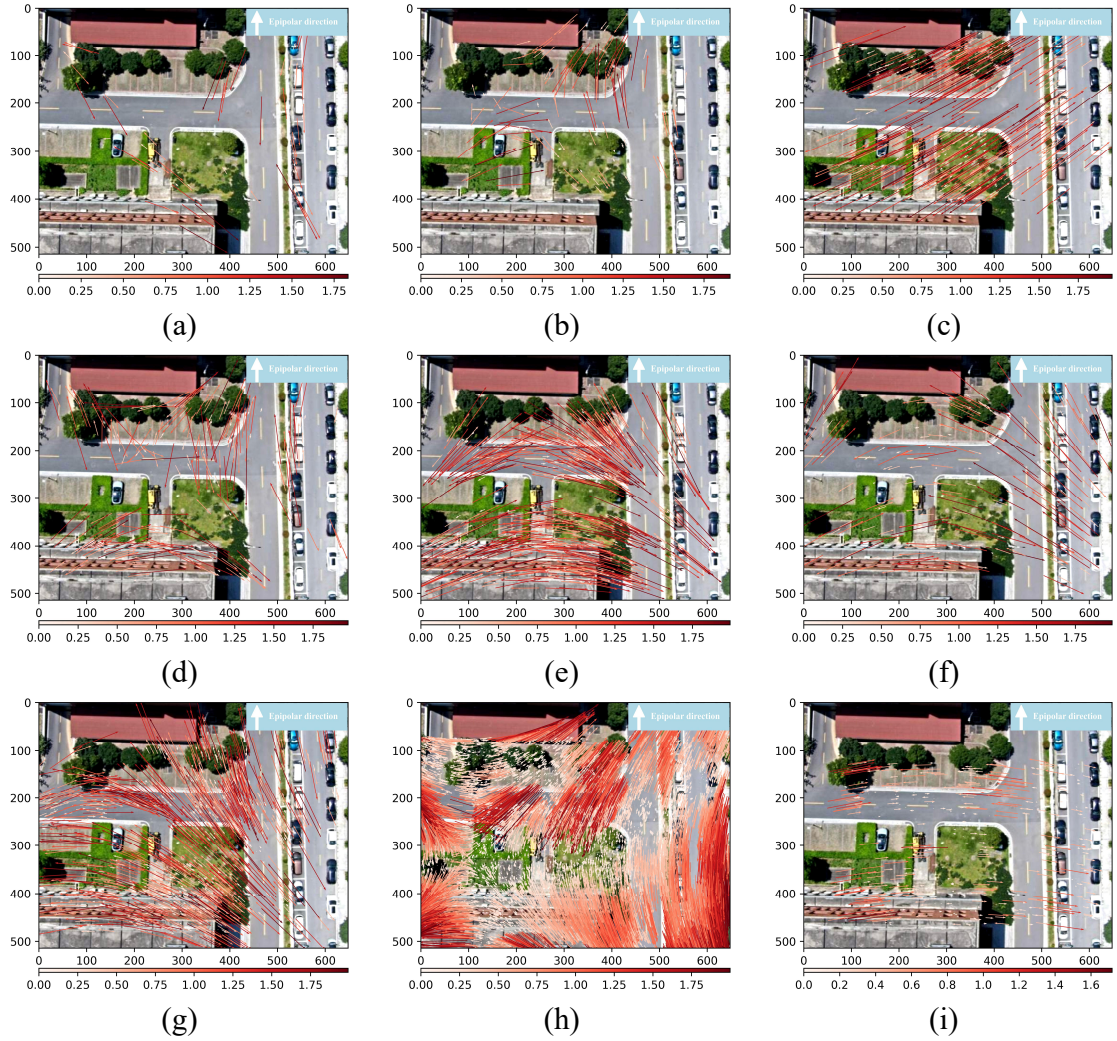


Fig. 8. The distribution of the residuals of the reprojection of the fundamental matrix of the nine methods on UAV data 2. The direction of the red arrow indicates the residual direction and size under the epipolar line constraint, and the color intensity indicates the residual size. The epipolar line direction is roughly consistent with the baseline direction. (a)HOPC results. (b)CFOG results. (c)RIFT results. (d)HAPCG results. (e)OFM results. (f)SuperGlue results. (g)LOFTR results. (h) RoMa results. (i) PCWLAD results.

Regarding NCM, RoMa matched quite dense points, and LoFTR, OFM, and HAPCG also achieved relatively high values. Due to their very low CMR, RIFT and SuperGlue produced the fewest correct matches. HOPC and CFOG also matched a limited number of points, with an average of approximately 140. In contrast, the proposed PCWLAD method achieved an average of around 610 correct matches, even with only 1,000 features extracted, significantly more than the area-based methods HOPC and CFOG. In our software implementation, the number of extracted features is provided as a configurable input parameter, allowing users to adjust it according to different application needs.

Quantitative results indicate that area-based methods such as HOPC and CFOG are capable of matching optical multimodal images with nonlinear intensity differences (NID); however, their limited number of matching points and offered integer pixel matching results accuracy make them unsuitable for applications requiring high-precision geometric calibration. Feature-based methods such as OFM and HAPCG can match more matches. However, their results require further outlier

removal, and their accuracy remains insufficient for precise geometric processing of optical imagery. RIFT produces a high proportion of gross errors. The deep learning-based method LoFTR achieves the highest number of matched points, though its accuracy is slightly lower than that of area-based methods like CFOG. SuperGlue shows a very low CMR, making it less reliable. RoMa demonstrates strong performance, high accuracy, and many points. In contrast, the proposed PCWLAD method demonstrates strong robustness across all three datasets, achieving the highest CMR and matching accuracy.

The relatively low number of matching points in CFOG and HOPC stems from their extraction of no more than 200 points and their reliance on integer pixel matching using the NCC criterion, which limits accuracy. On well-registered datasets with minimal geometric deformation, these methods can match nearly 200 points. However, under real UAV data conditions where geometric distortions are more pronounced, their NCM drops sharply. As illustrated in Figure 5(a), the assumption that larger template windows lead to higher

matching accuracy does not hold when geometric deformation is present. For feature-based methods such as OFM and HAPCG, the leading causes of low accuracy are noise and nonlinear intensity differences in the PC map. These factors compromise the repeatability of feature extraction using detectors like HARRIS [72] and FAST, often resulting in pixel-level deviations. Furthermore, although the descriptor is designed to enhance robustness against nonlinear radiometric differences by reducing dimensionality through filtering, this process also diminishes the distinctiveness of the descriptor. Nevertheless, feature-based methods can offer valuable coarse initial estimates, which help shorten the runtime of area-based matching and improve the overall matching success rate. SuperGlue incorporates structural relationships between keypoints in deep learning-based methods, significantly enhancing robustness. However, its CMR remains very low due to the susceptibility of the SuperPoint detector to PC map

noise. LoFTR, in contrast, excels in textureless regions and can produce dense matches. It employs a Transformer to bridge modality differences and supports sub-pixel matching accuracy. However, LoFTR may not generalize well to remote sensing data, as its training is not specifically targeted at such imagery. As a result, it exhibits gross errors and reduced robustness in data migration, although it performs better in near-field conditions, as shown in Table I. The PCWLAD method effectively addresses these limitations by incorporating noise characteristics and comprehensive structural information from the PC map. Leveraging the SSIM criterion achieves a higher CMR, while the WLAD framework suppresses noise interference during parameter estimation, enabling the accurate recovery of sub-pixel offsets. As a result, the method delivers high-precision matching performance for optical multimodal images.

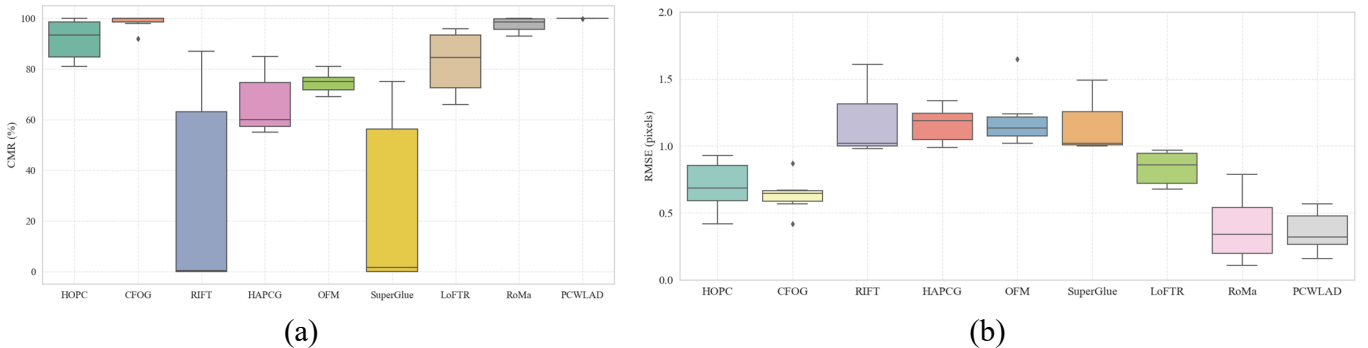


Fig. 9. The box plot provides a quantitative comparison of different metrics across various datasets. (a) CMR results. (b) RMSE results.

TABLE I
TEST RESULTS OF DIFFERENT METHODS ON VARIOUS DATASETS

Data	Landsat data			BGRNIR data			UAV data		
	NCM	CMR	RMSE	NCM	CMR	RMSE	NCM	CMR	RMSE
HOPC	200	100%	0.52	133	81%	0.68	77	93%	0.91
CFOG	199	100%	0.51	160	96%	0.65	84	98%	0.77
RIFT	5	0.4%	1.61	0	0	-	391	85%	1.00
HAPCG	1019	57%	1.30	1870	58%	1.19	206	80%	1.00
OFM	1641	72%	1.44	3215	73%	1.13	665	78%	1.05
SuperGlue	4	0.2%	1.49	0	0	-	172	75%	1.01
LoFTR	3062	95%	0.82	5427	69%	0.74	717	69%	0.96
RoMa	10000	100%	0.16	9700	97%	0.35	9550	95%	0.70
PCWLAD	800	100%	0.21	607	99%	0.43	413	100%	0.4

V. CONCLUSION

This study proposes a sub-pixel matching method for optical multimodal images, called PCWLAD. The PCWLAD framework consists of two main steps: coarse matching and precision optimization. A PC map without noise suppression is

used in the coarse matching stage, and the SSIM coefficient serves as the matching criterion. For precision optimization, sub-pixel displacement is accurately estimated through mutual structure weighting and the WLAD criterion. The method is evaluated on three types of multimodal optical images. PCWLAD demonstrates significant advantages in both CMR

and RMSE, and outperforms seven state-of-the-art methods regarding internal consistency and matching precision.

However, PCWLAD is less effective when dealing with large geometric deformations. Since template matching relies on good initial alignment, significant rotations and scale variations can lead to failure or require a larger search range. Fortunately, remote sensing images typically come with accurate georeferencing, which can be used for rough alignment to alleviate this issue. A more effective solution is

ACKNOWLEDGMENT

This study was supported by the National Natural Science Foundation of China (No. 42271410).

REFERENCES

- [1] C. Jiang *et al.*, "M2FNet: Multi-modal fusion network for object detection from visible and thermal infrared images," *International Journal of Applied Earth Observation and Geoinformation*, vol. 130, p. 103918, 2024/06/01/ 2024, doi: <https://doi.org/10.1016/j.jag.2024.103918>.
- [2] W. Huang, T. Li, J. Liu, P. Xie, S. Du, and F. Teng, "An overview of air quality analysis by big data techniques: Monitoring, forecasting, and traceability," *Information Fusion*, vol. 75, pp. 28-40, 2021/11/01/ 2021, doi: <https://doi.org/10.1016/j.inffus.2021.03.010>.
- [3] N. Chandra and H. Vaidya, "Automated detection of landslide events from multi-source remote sensing imagery: Performance evaluation and analysis of YOLO algorithms," *Journal of Earth System Science*, vol. 133, no. 3, p. 127, 2024.
- [4] L. Zhao *et al.*, "Geometric accuracy evaluation and analysis of ZY-1 02E IRS thermal infrared image data using GCP extraction based on phase correlation matching method," *The International Archives of the Photogrammetry, Remote Sensing and Spatial Information Sciences*, vol. 48, pp. 895-901, 2024.
- [5] M. A. Wulder *et al.*, "Fifty years of Landsat science and impacts," *Remote Sensing of Environment*, vol. 280, p. 113195, 2022/10/01/ 2022, doi: <https://doi.org/10.1016/j.rse.2022.113195>.
- [6] Y. Zhao and Y. Li, "Technical Characteristics and Application of Visible and Infrared Multispectral Imager," 2021, pp. 197-208.
- [7] Q. Fu *et al.*, "Analysis of multispectral polarization imaging image information based on micro-polarizer array," *Plos one*, vol. 19, no. 1, p. e0296397, 2024.
- [8] Z. Hu *et al.*, "Wide-swath and high-resolution whisk-broom imaging and on-orbit performance of SDGSAT-1 thermal infrared spectrometer," *Remote Sensing of Environment*, vol. 300, p. 113887, 2024/01/01/ 2024, doi: <https://doi.org/10.1016/j.rse.2023.113887>.
- [9] J. Ma, Y. Ma, and C. Li, "Infrared and visible image fusion methods and applications: A survey," *Information Fusion*, vol. 45, pp. 153-178, 2019/01/01/ 2019, doi: <https://doi.org/10.1016/j.inffus.2018.02.004>.
- [10] Y. Zhong *et al.*, "Pipeline leakage detection for district heating systems using multisource data in mid- and high-latitude regions," *ISPRS Journal of Photogrammetry and Remote Sensing*, vol. 151, pp. 207-222, 2019/05/01/ 2019, doi: <https://doi.org/10.1016/j.isprsjprs.2019.02.021>.
- [11] S. Motayyeb, F. Samadzadegan, F. D. Javan, and H. Hosseinpour, "Fusion of UAV-based infrared and visible images for thermal leakage map generation of building facades," *Heliyon*, vol. 9, no. 3, 2023.
- [12] M. Maimaitijiang, V. Sagan, P. Sidike, S. Hartling, F. Esposito, and F. B. Fritschi, "Soybean yield prediction from UAV using multimodal data fusion and deep learning," *Remote Sensing of Environment*, vol. 237, p. 111599, 2020/02/01/ 2020, doi: <https://doi.org/10.1016/j.rse.2019.111599>.
- [13] Y. He *et al.*, "Infrared machine vision and infrared thermography with deep learning: A review," *Infrared Physics & Technology*, vol. 116, p. 103754, 2021/08/01/ 2021, doi: <https://doi.org/10.1016/j.infrared.2021.103754>.

to integrate PCWLAD with feature-based matching methods, using the initial matches to provide better orientation and offset estimates. This reduces the search space and improves robustness to deformation, enabling the process to handle geometric and radiometric variations while maintaining high-precision matching. Future work will focus on enhancing feature detection in PC images, aiming to improve feature repeatability and the sub-pixel accuracy of the extracted points.

- [14] D. G. Lowe, "Distinctive Image Features from Scale-Invariant Keypoints," *International Journal of Computer Vision*, vol. 60, no. 2, pp. 91-110, 2004/11/01 2004, doi: 10.1023/B:VISI.0000029664.99615.94.
- [15] J. Li, Q. Hu, and M. Ai, "RIFT: Multi-Modal Image Matching Based on Radiation-Variation Insensitive Feature Transform," *IEEE Transactions on Image Processing*, vol. PP, pp. 1-1, 12/17 2019, doi: 10.1109/TIP.2019.2959244.
- [16] Z. Fan, M. Wang, Y. Pi, Y. Liu, and H. Jiang, "A Robust Oriented Filter-Based Matching Method for Multisource, Multitemporal Remote Sensing Images," *IEEE Transactions on Geoscience and Remote Sensing*, vol. 61, pp. 1-16, 2023, doi: 10.1109/TGRS.2023.3288531.
- [17] P. Kovese, "Image Features from Phase Congruency," 1995.
- [18] J. Malik, G. Sainarayanan, and R. Dahiya, "Corner Detection using Phase Congruency Features," in *2010 International Conference on Signal and Image Processing*, 15-17 Dec. 2010 2010, pp. 217-221, doi: 10.1109/ICSP.2010.5697472.
- [19] B. Zitová and J. Flusser, "Image registration methods: a survey," *Image and Vision Computing*, vol. 21, no. 11, pp. 977-1000, 2003/10/01/ 2003, doi: [https://doi.org/10.1016/S0262-8856\(03\)00137-9](https://doi.org/10.1016/S0262-8856(03)00137-9).
- [20] J.-C. Yoo and T. H. Han, "Fast Normalized Cross-Correlation," *Circuits, Systems and Signal Processing*, vol. 28, no. 6, pp. 819-843, 2009/12/01 2009, doi: 10.1007/s00034-009-9130-7.
- [21] D. Loeckx, P. Slagmolen, F. Maes, D. Vandermeulen, and P. Suetens, "Nonrigid Image Registration Using Conditional Mutual Information," *IEEE Transactions on Medical Imaging*, vol. 29, no. 1, pp. 19-29, 2010, doi: 10.1109/TMI.2009.2021843.
- [22] Y. Ye, J. Shan, L. Bruzzone, and L. Shen, "Robust Registration of Multimodal Remote Sensing Images Based on Structural Similarity," *IEEE Transactions on Geoscience and Remote Sensing*, vol. 55, no. 5, pp. 2941-2958, 2017, doi: 10.1109/tgrs.2017.2656380.
- [23] Y. Ye, B. Zhu, T. Tang, C. Yang, Q. Xu, and G. Zhang, "A robust multimodal remote sensing image registration method and system using steerable filters with first- and second-order gradients," *ISPRS Journal of Photogrammetry and Remote Sensing*, vol. 188, pp. 331-350, 2022/06/01/ 2022, doi: <https://doi.org/10.1016/j.isprsjprs.2022.04.011>.
- [24] Z. Wang and A. C. Bovik, "Mean squared error: Love it or leave it? A new look at Signal Fidelity Measures," *IEEE Signal Processing Magazine*, vol. 26, no. 1, pp. 98-117, 2009, doi: 10.1109/MSP.2008.930649.
- [25] A. Gruen, "Development and status of image matching in photogrammetry," *The Photogrammetric Record*, vol. 27, no. 137, pp. 36-57, 2012.
- [26] X. Jiang, J. Ma, G. Xiao, Z. Shao, and X. Guo, "A review of multimodal image matching: Methods and applications," *Information Fusion*, vol. 73, pp. 22-71, 2021/09/01/ 2021, doi: <https://doi.org/10.1016/j.inffus.2021.02.012>.
- [27] L. Meng *et al.*, "A robust registration method for UAV thermal infrared and visible images taken by dual-cameras," *ISPRS Journal of Photogrammetry and Remote Sensing*, vol. 192, pp. 189-214, 2022/10/01/ 2022, doi: <https://doi.org/10.1016/j.isprsjprs.2022.08.018>.
- [28] H. H. Chang, G. L. Wu, and M. H. Chiang, "Remote Sensing Image Registration Based on Modified SIFT and Feature Slope Grouping," *IEEE Geoscience and Remote Sensing Letters*, vol. 16, no. 9, pp. 1363-1367, 2019, doi: 10.1109/LGRS.2019.2899123.
- [29] Y. Xiang, F. Wang, and H. You, "OS-SIFT: A robust SIFT-like algorithm for high-resolution optical-to-SAR image registration in

- suburban areas," *IEEE Transactions on Geoscience and Remote Sensing*, vol. 56, no. 6, pp. 3078-3090, 2018.
- [30] K. Mikołajczyk and C. Schmid, "A performance evaluation of local descriptors," *IEEE Transactions on Pattern Analysis and Machine Intelligence*, vol. 27, no. 10, pp. 1615-1630, 2005, doi: 10.1109/TPAMI.2005.188.
- [31] X. Xiong, Q. Xu, G. Jin, H. Zhang, and X. Gao, "Rank-Based Local Self-Similarity Descriptor for Optical-to-SAR Image Matching," *IEEE Geoscience and Remote Sensing Letters*, vol. 17, no. 10, pp. 1742-1746, 2020, doi: 10.1109/LGRS.2019.2955153.
- [32] W. Ma *et al.*, "Remote Sensing Image Registration With Modified SIFT and Enhanced Feature Matching," *IEEE Geoscience and Remote Sensing Letters*, vol. 14, no. 1, pp. 3-7, 2017, doi: 10.1109/LGRS.2016.2600858.
- [33] D. Sengupta, P. Gupta, and A. Biswas, "A survey on mutual information based medical image registration algorithms," *Neurocomputing*, vol. 486, pp. 174-188, 2022/05/14/ 2022, doi: <https://doi.org/10.1016/j.neucom.2021.11.023>.
- [34] Y. Hel-Or, H. Hel-Or, and E. David, "Matching by Tone Mapping: Photometric Invariant Template Matching," *IEEE Transactions on Pattern Analysis and Machine Intelligence*, vol. 36, no. 2, pp. 317-330, 2014, doi: 10.1109/TPAMI.2013.138.
- [35] J. Revaud, P. Weinzaepfel, Z. Harchaoui, and C. Schmid, "DeepMatching: Hierarchical Deformable Dense Matching," *International Journal of Computer Vision*, vol. 120, no. 3, pp. 300-323, 2016/12/01 2016, doi: 10.1007/s11263-016-0908-3.
- [36] P. Weinzaepfel, J. Revaud, Z. Harchaoui, and C. Schmid, "DeepFlow: Large Displacement Optical Flow with Deep Matching," in *2013 IEEE International Conference on Computer Vision*, 1-8 Dec. 2013 2013, pp. 1385-1392, doi: 10.1109/ICCV.2013.175.
- [37] S. Fischer, F. Šroubek, L. Perrinet, R. Redondo, and G. Cristóbal, "Self-Invertible 2D Log-Gabor Wavelets," *International Journal of Computer Vision*, vol. 75, no. 2, pp. 231-246, 2007/11/01 2007, doi: 10.1007/s11263-006-0026-8.
- [38] C. A. Aguilera, A. D. Sappa, and R. Toledo, "LGHD: A feature descriptor for matching across non-linear intensity variations," in *2015 IEEE International Conference on Image Processing (ICIP)*, 27-30 Sept. 2015 2015, pp. 178-181, doi: 10.1109/ICIP.2015.7350783.
- [39] Z. Hou, Y. Liu, and L. Zhang, "POS-GIFT: A geometric and intensity-invariant feature transformation for multimodal images," *Information Fusion*, vol. 102, p. 102027, 2024.
- [40] Y. Yao, Y. Zhang, Y. Wan, X. Liu, and H. Guo, "Heterologous Images Matching Considering Anisotropic Weighted Moment and Absolute Phase Orientation," *Geomatics and Information Science of Wuhan University*, vol. 46, no. 11, pp. 1727-1736, 2021, doi: 10.13203/j.whugis20200702.
- [41] Z. Fan *et al.*, "3MRS: an effective coarse-to-fine matching method for multimodal remote sensing imagery," *Remote Sensing*, vol. 14, no. 3, p. 478, 2022.
- [42] A. Gruen, "Adaptive least squares correlation: a powerful image matching technique," *South African Journal of Photogrammetry, Remote Sensing and Cartography*, vol. 14, no. 3, pp. 175-187, 1985.
- [43] A. Sedaghat and H. Ebadi, "Accurate Affine Invariant Image Matching Using Oriented Least Square," *Photogrammetric Engineering & Remote Sensing*, vol. 81, no. 9, pp. 733-743, 2015, doi: 10.14358/pers.81.9.733.
- [44] D. Shin and J.-P. Muller, "Progressively weighted affine adaptive correlation matching for quasi-dense 3D reconstruction," *Pattern Recognition*, vol. 45, no. 10, pp. 3795-3809, 2012, doi: 10.1016/j.patcog.2012.03.023.
- [45] W. Ma *et al.*, "A collaborative correlation-matching network for multimodality remote sensing image classification," *IEEE Transactions on Geoscience and Remote Sensing*, vol. 60, pp. 1-18, 2022.
- [46] L. Xinghua, A. Wenhao, F. Ruitao, and L. Shaojie, "Survey of remote sensing image registration based on deep learning," *National Remote Sensing Bulletin*, vol. 27, no. 2, pp. 267-284, 2023, doi: 10.11834/jrs.20235012.
- [47] T. Nguyen, S. W. Chen, S. S. Shivakumar, C. J. Taylor, and V. Kumar, "Unsupervised Deep Homography: A Fast and Robust Homography Estimation Model," *IEEE Robotics and Automation Letters*, vol. 3, no. 3, pp. 2346-2353, 2018, doi: 10.1109/LRA.2018.2809549.
- [48] X. Zhang, C. Leng, Y. Hong, Z. Pei, I. Cheng, and A. Basu, "Multimodal Remote Sensing Image Registration Methods and Advancements: A Survey," *Remote Sensing*, vol. 13, no. 24, p. 5128, 2021. [Online]. Available: <https://www.mdpi.com/2072-4292/13/24/5128>.
- [49] Z. Ye *et al.*, "Visible-Infrared Images Matching Based on Deep Learning," in *Man-Machine-Environment System Engineering*, Singapore, S. Long, B. S. Dhillon, and L. Ye, Eds., 2024// 2024: Springer Nature Singapore, pp. 474-479.
- [50] F. Ye, Y. Su, H. Xiao, X. Zhao, and W. Min, "Remote Sensing Image Registration Using Convolutional Neural Network Features," *IEEE Geoscience and Remote Sensing Letters*, vol. 15, no. 2, pp. 232-236, 2018, doi: 10.1109/LGRS.2017.2781741.
- [51] M. Uss, B. Vozel, V. Lukin, and K. Chehdi, "Exhaustive search of correspondences between multimodal remote sensing images using convolutional neural network," *Sensors*, vol. 22, no. 3, p. 1231, 2022.
- [52] P.-E. Sarlin, D. DeTone, T. Malisiewicz, and A. Rabinovich, "Superglue: Learning feature matching with graph neural networks," in *Proceedings of the IEEE/CVF conference on computer vision and pattern recognition*, 2020, pp. 4938-4947.
- [53] P. Lindenberger, P. E. Sarlin, and M. Pollefeys, "LightGlue: Local Feature Matching at Light Speed," in *2023 IEEE/CVF International Conference on Computer Vision (ICCV)*, 1-6 Oct. 2023 2023, pp. 17581-17592, doi: 10.1109/ICCV51070.2023.01616.
- [54] S. Kim, M. Pollefeys, and D. Barath, "Learning to Make Keypoints Sub-Pixel Accurate," *arXiv preprint arXiv:2407.11668*, 2024.
- [55] L. H. Hughes, D. Marcos, S. Lobry, D. Tuia, and M. Schmitt, "A deep learning framework for matching of SAR and optical imagery," *ISPRS Journal of Photogrammetry and Remote Sensing*, vol. 169, pp. 166-179, 2020/11/01/ 2020, doi: <https://doi.org/10.1016/j.isprsjprs.2020.09.012>.
- [56] J. Sun, Z. Shen, Y. Wang, H. Bao, and X. Zhou, "LoFTR: Detector-free local feature matching with transformers," in *Proceedings of the IEEE/CVF conference on computer vision and pattern recognition*, 2021, pp. 8922-8931.
- [57] A. Aggarwal, M. Mittal, and G. Battineni, "Generative adversarial network: An overview of theory and applications," *International Journal of Information Management Data Insights*, vol. 1, no. 1, p. 100004, 2021.
- [58] J. Edstedt, Q. Sun, G. Bökman, M. Wadenbäck, and M. Felsberg, "RoMa: Robust Dense Feature Matching," in *2024 IEEE/CVF Conference on Computer Vision and Pattern Recognition (CVPR)*, 16-22 June 2024 2024, pp. 19790-19800, doi: 10.1109/CVPR52733.2024.01871.
- [59] M. Oquab *et al.*, "Dinov2: Learning robust visual features without supervision," *arXiv preprint arXiv:2304.07193*, 2023.
- [60] J. Ren, X. Jiang, Z. Li, D. Liang, X. Zhou, and X. Bai, "Minima: Modality invariant image matching," in *Proceedings of the Computer Vision and Pattern Recognition Conference*, 2025, pp. 23059-23068.
- [61] D. G. Viswanathan, "Features from accelerated segment test (fast)," in *Proceedings of the 10th workshop on image analysis for multimedia interactive services, London, UK*, 2009, pp. 6-8.
- [62] T. Huang, H. Pan, and N. Zhou, "Adaptive parameter local consistency automatic outlier removal algorithm for area-based matching," *ISPRS Ann. Photogramm. Remote Sens. Spatial Inf. Sci.*, vol. X-1-2024, pp. 99-106, 2024, doi: 10.5194/isprs-annals-X-1-2024-99-2024.
- [63] P. Kovesi, "Image features from phase congruency," *Videre: Journal of computer vision research*, vol. 1, no. 3, pp. 1-26, 1999.
- [64] X. Shen, C. Zhou, L. Xu, and J. Jia, "Mutual-Structure for Joint Filtering," in *2015 IEEE International Conference on Computer Vision (ICCV)*, 7-13 Dec. 2015 2015, pp. 3406-3414, doi: 10.1109/ICCV.2015.389.
- [65] I. Daubechies, R. DeVore, M. Fornasier, and C. S. n. Güntürk, "Iteratively reweighted least squares minimization for sparse recovery," *Communications on Pure and Applied Mathematics*, vol. 63, no. 1, pp. 1-38, 2010/01/01 2010, doi: <https://doi.org/10.1002/cpa.20303>.
- [66] J. C. Tilton, G. Lin, and B. Tan, "Measurement of the Band-to-Band Registration of the SNPP VIIRS Imaging System From On-

- Orbit Data," *IEEE Journal of Selected Topics in Applied Earth Observations and Remote Sensing*, vol. 10, no. 3, pp. 1056-1067, 2017, doi: 10.1109/JSTARS.2016.2601561.
- [67]J. C. Tilton, R. E. Wolfe, G. Lin, and J. J. Dellomo, "On-Orbit Measurement of the Effective Focal Length and Band-to-Band Registration of Satellite-Borne Whiskbroom Imaging Sensors," *IEEE Journal of Selected Topics in Applied Earth Observations and Remote Sensing*, vol. 12, no. 11, pp. 4622-4633, 2019, doi: 10.1109/JSTARS.2019.2949677.
- [68]M. Brown and S. Süsstrunk, "Multi-spectral SIFT for scene category recognition," in *CVPR 2011*, 20-25 June 2011 2011, pp. 177-184, doi: 10.1109/CVPR.2011.5995637.
- [69]J. L. Schönberger and J. M. Frahm, "Structure-from-Motion Revisited," in *2016 IEEE Conference on Computer Vision and Pattern Recognition (CVPR)*, 27-30 June 2016 2016, pp. 4104-4113, doi: 10.1109/CVPR.2016.445.
- [70]D. Barath, D. Mishkin, M. Polic, W. Förstner, and J. Matas, "A Large-Scale Homography Benchmark," in *2023 IEEE/CVF Conference on Computer Vision and Pattern Recognition (CVPR)*, 17-24 June 2023 2023, pp. 21360-21370, doi: 10.1109/CVPR52729.2023.02046.
- [71]M. A. Fischler and R. C. Bolles, "Random sample consensus: a paradigm for model fitting with applications to image analysis and automated cartography," *Commun. ACM*, vol. 24, pp. 381-395, 1981.
- [72]K. G. Derpanis, "The harris corner detector," *York University*, vol. 2, no. 1, p. 2, 2004.